Available online at www.sciencedirect.com
SCIENCE DIRECT®
Journal of Mechanics and Physics of solids
53 (2005) 91–121
JOURNAL OF THE MECHANICS AND PHYSICS OF SOLIDS
www.elsevier.com/locate/jmps

A material force method for inelastic fracture mechanics

T.D. Nguyen[a,*], S. Govindjee[b], P.A. Klein[c], H. Gao[d]

[a]*Division of Mechanics and Computation, Department of Mechanical Engineering, Stanford University, Stanford, CA 94305, USA*
[b]*Structural Engineering, Mechanics and Materials, Department of Civil and Environmental Engineering, Berkeley, CA 94720, USA*
[c]*Science-Based Materials Modeling Department, Sandia National Laboratories, P.O. Box 0969, Livermore, CA 94551, USA*
[d]*Department of Theory of Mesoscopic Phenomena, Max-Planck Institute for Metals Research, Heisenbergstrasse 1, D-70569 Stuttgart, Germany*

Received 24 December 2003; accepted 7 June 2004

Abstract

A material force method is proposed for evaluating the energy release rate and work rate of dissipation for fracture in inelastic materials. The inelastic material response is characterized by an internal variable model with an explicitly defined free energy density and dissipation potential. Expressions for the global material and dissipation forces are obtained from a global balance of energy–momentum that incorporates dissipation from inelastic material behavior. It is shown that in the special case of steady-state growth, the global dissipation force equals the work rate of dissipation, and the global material force and *J*-integral methods are equivalent. For implementation in finite element computations, an equivalent domain expression of the global material force is developed from the weak form of the energy–momentum balance. The method is applied to model problems of cohesive fracture in a remote *K*-field for viscoelasticity and elastoplasticity. The viscoelastic problem is used to compare various element discretizations in combination with different schemes for computing

*Corresponding author now at Sandia National Laboratories, Livermore, CA.
E-mail address: tdnguye@sandia.gov (T.D. Nguyen).

0022-5096/$ - see front matter
doi:10.1016/j.jmps.2004.06.010

strain gradients. For the elastoplastic problem, the effects of cohesive and bulk properties on the plastic dissipation are examined using calculations of the global dissipation force.

Keywords: Material force; *J*-integral; Cohesive fracture; Viscoelastic fracture; Ductile fracture

1. Introduction

Dissipation from inelastic material behavior is an important consideration in many fracture problems. The significance of dissipation to fracture has been widely acknowledged since the early 1950's when Orowan (1952) and Irwin (1948) independently recognized that the largest contribution to the energy release rate in metals is not the intrinsic surface energy, as proposed earlier by Griffith (1920) for brittle materials, but the plastic dissipation induced by the concentration of stresses at the crack tip. The problem of dissipation is more difficult to characterize in small-scale applications such as the fracture of micro-electronic devices and bio-systems. When the size of the fracture process zone is large compared to the characteristic structural dimensions, the effects of dissipation exhibit a dependence on geometry and cannot be lumped into a material parameter like the plane-strain fracture toughness K_{IC}. For these applications, it becomes necessary to calculate independently the energy release rate and the work rate of dissipation accompanying crack growth.

A proven method for calculating the energy release rate in elastic materials is the *J*-integral. A comprehensive review of the *J*-integral and its variants is provided by Moran and Shih (1987). Here, we briefly mention that Rice (1968) demonstrated the path-independence of the *J*-integral and established its equivalence to the energy release rate for sharp and blunt cracks in nonlinear elastic materials. A similar method was proposed by Eshelby (1951,1956) for the driving force on dislocations in an elastic continuum. Eshelby (1970) recognized the use of the energy–momentum tensor in the *J*-integral and interpreted it in a broader context as a configurational force governing the motion of a material defect. Path-independence is an important property of the *J*-integral since it allows the energy release rate and the stress intensity factor to be determined from remote fields. While path-independence can be demonstrated in quasistatic problems for elastic materials, the property exists for inelastic materials only under certain stringent conditions. For example, application of the *J*-integral to rate-independent elastoplasticity is limited to monotonic loading of static cracks to prevent material unloading in the plastic zone. For stationary cracks in a power-law creep material, Landes and Begley (1976) introduced an analogous rate integral C^* that is path-independent under steady-state (long-time) conditions. Freund and Hutchinson (1985) proposed that if the energy measure in the energy–momentum tensor were interpreted more generally as the stress work density then the *J*-integral would be path-independent for steady-state (constant velocity) crack growth regardless of the material response.

A number of path-domain integrals have been developed to extend the J-integral approach to inelastic fracture under general loading conditions. Examples include the family of T^* integrals developed by Brust et al. (1985,1986), Brust and Atluri (1986), the J^*-integral of Blackburn (1972), and the $\hat{J}$-integral of Kishimoto et al. (1980). These integrals differ mostly in the energy measure used in defining the energy–momentum tensor. For $\hat{J}$, application of the elastic strain energy density results in a domain term that contains the product of the stress and gradient of inelastic strain. For perfect plasticity, this domain term can be interpreted as the work rate of plastic dissipation.

In this paper, we seek to develop a more general method for determining the energy release rate in the presence of dissipation in the bulk material. As a starting point, we return to the framework introduced by Eshelby (1970) for the configurational force acting on a material defect. The topic of configurational forces with regards to fracture has been re-invigorated in recent years by the efforts Stumpf and Le (1990), Maugin and Trimarco (1992), and Steinmann (2000) to formalize the variational context of the material (inverse) motion problem. In the material motion problem, material coordinates are the unknown variables, and configurational forces, also referred to as material forces, are the thermodynamic conjugates of material motions. Material forces also arise in the presence of material inhomogeneities and defects such as cracks. Under quasi-static conditions, the global material force for a crack in a homogeneous, elastic body is equal to the path-independent, vectorial J-integral. Simo and Honein (1990) developed a more general path-domain integral from a discrete variational formulation for elastoplasticity and elasto-viscoplasticity based on the principal of maximum dissipation. They related the path-domain integral to the discrete energy release rate and the domain term specifically to the work rate of incremental plastic dissipation.

The material force framework affords a uniform treatment of complex material behavior in fracture. This has enabled recent applications to thermoelastic (Maugin and Berezovski, 1999), elastic-electromagnetic (Maugin et al., 1992), and isotropic continuum damage (Liebe et al., 2003) material models. The effect of material behavior is introduced through the free energy density part of the energy–momentum tensor as discussed by Simo and Honein (1990) and Maugin and Trimarco (1992). For materials exhibiting mechanical dissipation, the free energy density is expressed in terms of the total and internal (inelastic) strains. This leads to the addition of body forces associated with the material gradient of the inelastic strains to the local energy–momentum balance. In what follows, we demonstrate that the presence of inelastic body forces obviates the path-independence property of the resulting material force expression. However, it permits direct evaluation of the work rate of dissipation associated with crack growth. This trade-off yields a formulation for calculating the energy release rate that demands fewer restrictions on the material model and crack motion than J-integral based methods. The formulation requires only that the constitutive relations are derived from a free energy density, and that the time evolution of the inelastic strains conforms to a dissipation potential. Given

these conditions, the material force method can be used for arbitrary transient fracture problems. For the special case of steady-state growth, it can be shown that the material force and path-independent J-integral methods calculate the same work rate balance.

The first section provides a concrete application of the material force framework proposed by Maugin and Trimarco (1992) to fracture in inelastic materials. Specifically, a formulation is developed for a crack in a homogeneous, linear viscoelastic body, and a method is proposed for implementation in a finite element setting. The presentation is restricted to small-strains for a simpler, less cluttered formulation. This facilitates physical interpretation and enables direct comparison to the generalized J-integral of Freund and Hutchinson (1985). The formulation can be extended readily to finite deformation as demonstrated by Govindjee (2004) for nonlinear viscoelasticity. The presentation begins with a brief material description. Then from the local statement of physical momentum balance, a local and global balance of energy–momentum is presented that accounts for dissipation from the inelastic material response. An expression for the global material force is obtained from the global energy–momentum balance. It consists of a contour integral of material traction acting on the external boundary less a volume integral of the inelastic body force. The latter is defined as the global dissipation force. For numerical evaluation, an equivalent domain integral expression is obtained from the weak form of the energy–momentum balance for the global material force. Applying a Galerkin discretization yields corresponding nodal material and dissipation forces. Consideration is given to the discretization method, particularly to computing quantities involving strain gradients. In the next section, the material force method is adapted for associative elastoplasticity. The result is the time-continuous counterpart of the discrete path-domain integral developed by Simo and Honein (1990). The material model does not alter the mathematical formulation. Therefore, the presentation is focused on issues of physical interpretation and numerical implementation that are unique to plasticity.

In the final section, the material force method is applied to calculate the fracture energy and work rate of dissipation for cohesive fracture in an applied K-field for viscoelasticity and J_2 elastoplasticity. The cohesive energy provides a convenient check for the material force calculations. The viscoelastic problem is used to compare the choice of discretization methods in combination with various schemes for computing strain gradients. The elastoplastic problem is used to study the influence of cohesive and bulk properties on the plastic dissipation for crack initiation and steady-state growth. This problem was studied by Tvergaard and Hutchinson (1992), where they showed that the energy release rate at steady state as determined from the applied K-field varied sharply with the ratio of the cohesive and yield strengths, the hardening modulus, and the cohesive energy, and that the applied energy release rate at initiation depended only on the cohesive energy. Here, we examine these conclusions as they pertain to the plastic dissipation using the global dissipation force.

2. Material and dissipation forces for linear viscoelasticity

A material force method is developed for fracture in a homogeneous, viscoelastic solid. It is shown that the material force and J-integral methods calculate the same work rate balance for steady-state growth. Finally, a discretization method is proposed for implementation in a finite element setting.

2.1. Material description

The particular linear viscoelastic model considered here is a multi-dimensional generalization of the standard solid model shown in Fig. 1. A detailed description of viscoelasticity as an internal variable model can be found in Simo and Hughes (1998, Chapter 10). The description assumes an additive split of the strain tensor as

$$\boldsymbol{\varepsilon} = \boldsymbol{\varepsilon}^{\mathrm{e}} + \boldsymbol{\varepsilon}^{\mathrm{v}}, \tag{1}$$

where the viscous and elastic strains $\boldsymbol{\varepsilon}^{\mathrm{v}}$ and $\boldsymbol{\varepsilon}^{\mathrm{e}}$ are internal variables that characterize the state of material relaxation. Also assumed is a free energy density of the form

$$\Psi(\boldsymbol{\varepsilon}, \boldsymbol{\varepsilon}^{\mathrm{v}}) = \Psi^{\mathrm{EQ}}(\boldsymbol{\varepsilon}) + \Psi^{\mathrm{NEQ}}(\boldsymbol{\varepsilon} - \boldsymbol{\varepsilon}^{\mathrm{v}}), \tag{2}$$

where $\Psi^{\mathrm{EQ}}(\boldsymbol{\varepsilon})$ is a quadratic potential that prescribes the elastic, equilibrium behavior. The time-dependent, non-equilibrium behavior is given by the quadratic potential $\Psi^{\mathrm{NEQ}}(\boldsymbol{\varepsilon}^{\mathrm{e}})$. The stress response is obtained from the free energy density as

$$\boldsymbol{\sigma} = \frac{\partial \Psi}{\partial \boldsymbol{\varepsilon}} = \underbrace{\frac{\partial \Psi^{\mathrm{EQ}}}{\partial \boldsymbol{\varepsilon}}}_{\boldsymbol{\sigma}^{\mathrm{EQ}}} + \underbrace{\frac{\partial \Psi^{\mathrm{NEQ}}}{\partial \boldsymbol{\varepsilon}^{\mathrm{e}}}}_{\boldsymbol{\sigma}^{\mathrm{NEQ}}}. \tag{3}$$

A viscous dissipation potential is obtained from thermodynamic considerations as

$$\mathscr{D}^{\mathrm{visc}} = \boldsymbol{\sigma}^{\mathrm{NEQ}} : \dot{\boldsymbol{\varepsilon}}^{\mathrm{v}}. \tag{4}$$

For $\mathscr{D}^{\mathrm{visc}}$ to be positive, the following linear evolution is chosen

$$\boldsymbol{\eta} : \dot{\boldsymbol{\varepsilon}}^{\mathrm{v}} = \boldsymbol{\sigma}^{\mathrm{NEQ}}, \tag{5}$$

where $\boldsymbol{\eta}$ is a positive definite viscosity tensor.

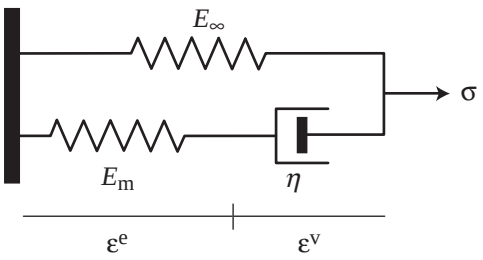

Fig. 1. Standard solid model where E_∞ is the long-time modulus, $E_m + E_\infty$ equals the short-time modulus, and η is the viscosity.

2.2. Balance of energy–momentum

In the material force framework, crack growth is treated formally as a change in the undeformed, material configuration. Thus, the distinction between the current and undeformed configurations, while seemingly superfluous in a small-strain setting, is essential to the formulation. Consider the undeformed configuration of a crack in an otherwise homogeneous, linear viscoelastic body as shown in Fig. 2. A planar geometry is assumed for convenience. The body is referred to as Ω_o, and a contour Γ_o with outward unit normal $\mathbf{N}$ is defined tracing the external boundary and the crack surfaces. It is joined to a similarly directed contour Γ_δ surrounding the infinitesimal volume Ω_δ containing the crack tip to define a closed path. In the following, the variable $\mathbf{X}$ refers to the coordinates of a material point in the undeformed configuration.

It is assumed that the physical motion problem has been solved such that the displacements $\mathbf{u}$ and physical stresses are known. Given these quantities, the material force driving crack growth is determined by considering the material motion problem. For a detailed treatment of material motion, refer to Maugin and Trimarco (1992), Steinmann (2000), and Govindjee and Mihalic (1996). In the absence of body forces, the local balance of physical momentum for a material point in Ω_o under quasi-static conditions is given by

$$\nabla \cdot \boldsymbol{\sigma} = \mathbf{0}. \tag{6}$$

Following Maugin and Trimarco (1992), the balance of energy–momentum is determined from Eq. (6) by contracting the equation with the transpose of the displacement gradient and then employing the definition of the Eshelbian

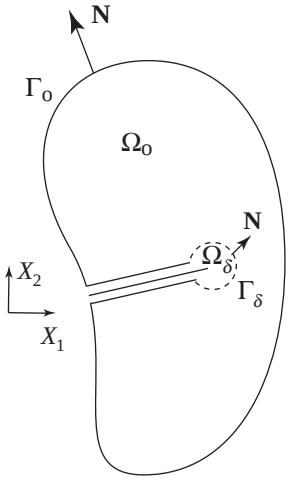

Fig. 2. A crack in an otherwise homogeneous body.

energy–momentum tensor for the viscoelastic material

$$\boldsymbol{\Sigma} = \Psi(\boldsymbol{\varepsilon}, \boldsymbol{\varepsilon}^{\mathrm{v}})\mathbf{1} - \boldsymbol{\nabla}\mathbf{u}^{\mathrm{T}}\boldsymbol{\sigma}, \tag{7}$$

where $\Psi(\boldsymbol{\varepsilon}, \boldsymbol{\varepsilon}^{\mathrm{v}})$ is the free energy density defined in Eq. (2). In the material motion problem $\boldsymbol{\Sigma}$ is also referred to as the material stress. This yields the intermediate result

$$\boldsymbol{\nabla} \cdot \boldsymbol{\Sigma} - \frac{\partial \Psi(\boldsymbol{\varepsilon}, \boldsymbol{\varepsilon}^{\mathrm{v}})}{\partial \boldsymbol{\varepsilon}} : \boldsymbol{\nabla}\boldsymbol{\varepsilon} - \frac{\partial \Psi(\boldsymbol{\varepsilon}, \boldsymbol{\varepsilon}^{\mathrm{v}})}{\partial \boldsymbol{\varepsilon}^{\mathrm{v}}} : \boldsymbol{\nabla}\boldsymbol{\varepsilon}^{\mathrm{v}} + \boldsymbol{\nabla}(\boldsymbol{\nabla}\mathbf{u}) : \boldsymbol{\sigma} = \mathbf{0}. \tag{8}$$

The terms of Eq. (8) are combined using the constitutive relations in Eq. (3) and the symmetry property of $\boldsymbol{\sigma}$ to obtain

$$\boldsymbol{\nabla} \cdot \boldsymbol{\Sigma} + \boldsymbol{\sigma}^{\mathrm{NEQ}} : \boldsymbol{\nabla}\boldsymbol{\varepsilon}^{\mathrm{v}} = \mathbf{0}. \tag{9}$$

Eq. (9) is a local balance statement of energy–momentum that relates the divergence of the energy–momentum tensor to a material body force. For the elastic problem, the body force vanishes and the energy–momentum tensor becomes divergence free. In this formulation, material inelasticity explicitly adds a material body force to the local balance statement. The body force is the product of the gradient of viscous strain and the non-equilibrium component of stress, and thus is referred to as the viscous body force.

The global balance of energy–momentum is obtained by integrating the local balance statement (9) over the regular part of the body defined as $\Omega_{\mathrm{r}} = \Omega_{\mathrm{o}} - \Omega_{\delta}$. To obtain a general formulation, the following development refrains from specifying material traction boundary conditions. Applying the divergence theorem and shrinking Ω_{δ} to the crack tip gives

$$\int_{\Gamma_{\mathrm{o}}} \boldsymbol{\Sigma}\mathbf{N}\,\mathrm{d}S - \lim_{\delta\to 0}\int_{\Omega_{\mathrm{r}}} -\boldsymbol{\sigma}^{\mathrm{NEQ}} : \boldsymbol{\nabla}\boldsymbol{\varepsilon}^{\mathrm{v}}\,\mathrm{d}V = \lim_{\delta\to 0}\int_{\Gamma_{\delta}} \boldsymbol{\Sigma}\mathbf{N}\,\mathrm{d}S. \tag{10}$$

When either $\boldsymbol{\sigma}^{\mathrm{NEQ}} = \mathbf{0}$ or $\boldsymbol{\nabla}\boldsymbol{\varepsilon}^{\mathrm{v}} = \mathbf{0}$ in Ω_{o}, the volume integral vanishes and the relationship in Eq. (10) reduces to a statement of path-independence for the elastic, vectorial J-integral. The contour integral on the right-hand side of Eq. (10) signifies the near-tip driving force while the expression forming the left-hand side is defined as the global material force

$$\mathbf{F}^{\mathrm{mat}} = \int_{\Gamma_{\mathrm{o}}} \boldsymbol{\Sigma}\mathbf{N}\,\mathrm{d}S - \underbrace{\lim_{\delta\to 0}\int_{\Omega_{\mathrm{r}}} -\boldsymbol{\sigma}^{\mathrm{NEQ}} : \boldsymbol{\nabla}\boldsymbol{\varepsilon}^{\mathrm{v}}\,\mathrm{d}V}_{\mathbf{F}^{\mathrm{dissip}}}. \tag{11}$$

The expression for $\mathbf{F}^{\mathrm{mat}}$ consists of a contour integral for the driving force supplied at the external boundary and a volume integral of the viscous body force evaluated between the external boundary and near-tip contour. The latter is defined as the global dissipation force $\mathbf{F}^{\mathrm{dissip}}$.

The limiting behavior of $\mathbf{F}^{\mathrm{dissip}}$ can be surmised from the energy–momentum balance in Eq. (10). Given physical loading conditions, the contour integral for the far-field driving force is finite. Assuming that the near-tip driving force is also finite, the global dissipation force, defined as the difference of two finite terms, must remain finite in the limit $\delta \to 0$. It can be shown that the contribution from the near-tip

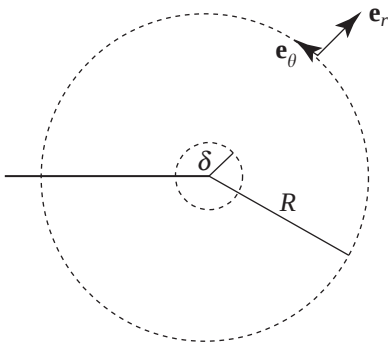

Fig. 3. An annular region centered about a sharp crack tip.

volume to $\mathbf{F}^{\text{dissip}}$ is zero for linear viscoelastic fracture problems. Clearly when the viscoelastic fields are non-singular in Ω_δ, the viscous dissipation integral over Ω_δ vanishes in the limit as the volume Ω_δ is shrunk to zero. For a sharp crack, when the asymptotic solution for $\boldsymbol{\sigma}^{\text{NEQ}}$ and $\boldsymbol{\varepsilon}^{\text{v}}$ exhibits an inverse square root singularity, the following shows that the viscous body force in the K-dominant zone does not contribute to $\mathbf{F}^{\text{dissip}}$. The integral for $\mathbf{F}^{\text{dissip}}$ for the K-dominant zone drawn in Fig. 3 can be written as

$$\lim_{\delta\to 0}\int_{-\pi}^{\pi}\int_{\delta}^{R}\boldsymbol{\sigma}^{\text{NEQ}}:\boldsymbol{\nabla}\boldsymbol{\varepsilon}^{\text{v}} r\,\mathrm{d}r\,\mathrm{d}\theta=\lim_{\delta\to 0}\int_{-\pi}^{\pi}\int_{\delta}^{R}\left[\frac{\mathrm{d}r}{r}\right]\boldsymbol{f}(\theta)\,\mathrm{d}\theta, \tag{12}$$

where r is the radial distance from the crack tip and $\boldsymbol{f}(\theta)$ is the angular variation of the viscous body force. The integral over r is undefined in the limit as $\delta\to 0$. However, the limit of $\mathbf{F}^{\text{dissip}}$ must be well defined since the near-tip driving force is finite. For the limit to exist, the integral for $\mathbf{F}^{\text{dissip}}$ over the K-dominant zone must equal zero. This is possible only if the integral over the angular variation $\boldsymbol{f}(\theta)$ in Eq. (12) vanishes.

2.3. Comparison to the J-integral for steady state, viscoelastic crack growth

The global material force can be viewed as a generalization of the elastic J-integral that incorporates the effects of viscous dissipation in the bulk material. It represents a different approach to material inelasticity than the generalized J-integral of Freund and Hutchinson (1985). The contour integral proposed by Freund and Hutchinson can be written for quasi-static problems as

$$J=\int_{\Gamma_o}(UN_1-u_{i,1}\sigma_{ij}N_j)\,\mathrm{d}S, \tag{13}$$

where $\mathbf{e}_1$ is the growth direction, and U is the stress work density defined as,

$$U=\int_0^t\sigma_{ij}\dot{\varepsilon}_{ij}\,\mathrm{d}t. \tag{14}$$

Because the definition of stress work density is devoid of constitutive restrictions, path-independence can be demonstrated for the integral in Eq. (13) regardless of material behavior provided that growth is steady state. The material force formulation in contrast forgoes the concept of path-independence in favor of a direct accounting of dissipation in the bulk material. Consequently, its application is not limited to steady-state problems.

For the special case of steady-state growth, the material force and J-integral methods calculate the same work rate balance. To demonstrate this, it is shown first that the global dissipation force calculates the work rate of dissipation for steady-state growth. Consider a crack growing at a constant velocity, $\mathbf{v} = v\mathbf{e}_1$, as illustrated in Fig. 4. An additional reference frame $\hat{\mathbf{X}}$ is defined affixed to the crack tip. It is related to $\mathbf{X}$ by the translation $\hat{\mathbf{X}} = \mathbf{X} - \mathbf{v}t$ where t denotes the time. Hence, for any steady-state field $f(\mathbf{X}, t)$

$$\boldsymbol{\nabla}_{\mathbf{X}} f(\mathbf{X}, t) = \boldsymbol{\nabla}_{\hat{\mathbf{X}}} f(\hat{\mathbf{X}}), \qquad \frac{\partial f(\mathbf{X}, t)}{\partial t} = -v\boldsymbol{\nabla}_{\hat{\mathbf{X}}} f(\hat{\mathbf{X}}) \cdot \mathbf{e}_1. \tag{15}$$

The above relations allow the viscous dissipation potential in Eq. (4) to be redefined in the translating frame as

$$\mathscr{D}^{\text{visc}} = -v\boldsymbol{\sigma}^{\text{NEQ}} : (\boldsymbol{\nabla}\boldsymbol{\varepsilon}^{\text{v}} \cdot \mathbf{e}_1). \tag{16}$$

Rewriting the global energy–momentum balance in Eq. (10) in the translating frame using the steady-state result in Eq. (16) gives

$$\int_{\tilde{\Gamma}_{\text{o}}} \mathbf{e}_1 \cdot \boldsymbol{\Sigma}\mathbf{N}\,\mathrm{d}S - \frac{1}{v}\lim_{\delta\to 0}\int_{\tilde{\Omega}_{\text{r}}} \mathscr{D}^{\text{visc}}\,\mathrm{d}V = \lim_{\delta\to 0}\int_{\tilde{\Gamma}_{\delta}} \mathbf{e}_1 \cdot \boldsymbol{\Sigma}\mathbf{N}\,\mathrm{d}S, \tag{17}$$

where the superposed tilde accent refers to moving integration domains. This relation shows explicitly that the component of the global dissipation force in the growth direction computes the work rate of dissipation for a crack advancing at speed v. Then, the global balance of energy–momentum Eq. (17) expresses the

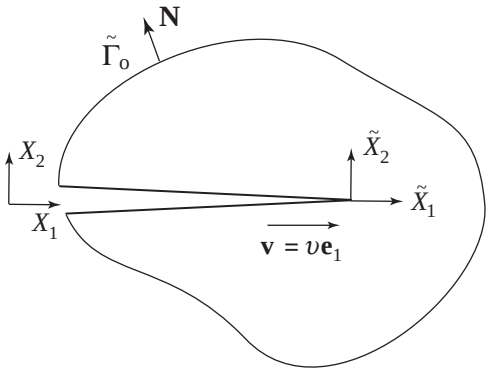

Fig. 4. Steady-state crack growth in a viscoelastic body.

following work rate balance:

$$G - W_{\text{dissip}} = G_\delta, \tag{18}$$

where G_δ and G are the near-tip and far-field energy release rate and W_{dissip} is the work rate of dissipation defined between the near-tip and far-field contours. The relationship (18) states that for a crack in a viscoelastic medium, only part of the far-field energy release rate supplied by the boundary conditions is delivered to the crack tip. The rest is lost in the bulk material to dissipation from inelastic processes.

The same work rate balance can be obtained from the generalized J-integral in Eq. (13). The rate of stress work density in Eq. (14) is expanded using the additive split of $\boldsymbol{\varepsilon}$ in Eq. (1) and $\boldsymbol{\sigma}$ in Eq. (3) as

$$\begin{aligned}\dot{U}(\boldsymbol{\varepsilon}) &= \boldsymbol{\sigma} : \dot{\boldsymbol{\varepsilon}},\\ &= \boldsymbol{\sigma}^{\text{EQ}} : \dot{\boldsymbol{\varepsilon}} + \boldsymbol{\sigma}^{\text{NEQ}} : \dot{\boldsymbol{\varepsilon}}^{\text{e}} + \boldsymbol{\sigma}^{\text{NEQ}} : \dot{\boldsymbol{\varepsilon}}^{\text{v}},\\ &= \dot{\Psi} + \boldsymbol{\sigma}^{\text{NEQ}} : \dot{\boldsymbol{\varepsilon}}^{\text{v}}.\end{aligned} \tag{19}$$

Equation (19) is transformed using the steady-state relations (15) as,

$$U_{,1} = \Psi_{,1} - \frac{1}{v}\mathscr{D}^{\text{visc}}. \tag{20}$$

Let $\tilde{\Gamma}_{\text{r}}$ be the closed contour surrounding the regular part of the body $\tilde{\Omega}_{\text{r}} = \tilde{\Omega}_{\text{o}} - \tilde{\Omega}_\delta$. The relationship in Eq. (20) and the divergence theorem are used to obtain the following intermediate result:

$$\begin{aligned}\int_{\tilde{\Gamma}_{\text{r}}} UN_1 \,\mathrm{d}S &= \int_{\tilde{\Omega}_{\text{r}}} U_{,1} \,\mathrm{d}V,\\ &= \int_{\tilde{\Omega}_{\text{r}}} \Psi_{,1} \,\mathrm{d}V - \frac{1}{v}\int_{\tilde{\Omega}_{\text{r}}} \mathscr{D}^{\text{visc}} \,\mathrm{d}V,\\ &= \int_{\tilde{\Gamma}_{\text{r}}} \Psi N_1 \,\mathrm{d}S - \frac{1}{v}\int_{\tilde{\Omega}_{\text{r}}} \mathscr{D}^{\text{visc}} \,\mathrm{d}V.\end{aligned} \tag{21}$$

Finally, the J-integral in Eq. (13) is evaluated along $\tilde{\Gamma}_{\text{r}}$ in the limit $\delta \to 0$. Applying the path-independence property and the intermediate result in Eq. (21) yields

$$\begin{aligned}&\lim_{\delta\to 0}\int_{\tilde{\Gamma}_{\text{r}}} (UN_1 - u_{i,1}\sigma_{ij}N_j)\,\mathrm{d}S = 0,\\ &\lim_{\delta\to 0}\int_{\tilde{\Gamma}_{\text{r}}} (\Psi N_1 - u_{i,1}\sigma_{ij}N_j)\,\mathrm{d}S - \frac{1}{v}\lim_{\delta\to 0}\int_{\tilde{\Omega}_{\text{r}}} \mathscr{D}^{\text{visc}}\,\mathrm{d}V = 0,\\ &\int_{\tilde{\Gamma}_{\text{o}}} \Sigma_{1j}N_j \,\mathrm{d}S - \frac{1}{v}\lim_{\delta\to 0}\int_{\tilde{\Omega}_{\text{r}}} \mathscr{D}^{\text{visc}}\,\mathrm{d}V = \lim_{\delta\to 0}\int_{\tilde{\Gamma}_\delta} \Sigma_{1j}N_j \,\mathrm{d}S,\end{aligned} \tag{22}$$

where the energy–momentum balance Eq. (17) for the crack growth direction is recovered by the ultimate relation in Eq. (22).

The main result of this section demonstrates that the material force and generalized J-integral methods calculate the same work rate balance for steady-state growth. The difference between the two formulations relates to more general

loading cases. Because the material force method explicitly accounts for dissipation, it can be used under arbitrary transient conditions. For the transient problem, the relationship between the global dissipation force and the work rate of dissipation must be inferred from the physical significance of the contour integral terms in the energy–momentum balance Eq. (10). Furthermore, the value calculated by the global dissipation force for the "large-scale yielding" case can include contributions unrelated to crack growth.

2.4. Numerical implementation

An equivalent domain integral expression for the global material force $\mathbf{F}^{\text{mat}}$ is developed for implementation in the finite element framework. The domain expression is obtained from the weak form of the material force balance. Inspired by the weight function used by the domain integral method (Li et al., 1985; Shih et al., 1986; Moran and Shih, 1987), a smooth test function $\mathbf{Q} \in \mathcal{Q}$ is chosen where $\mathcal{Q}$ is defined as

$$\mathcal{Q} = \{\mathbf{Q} = Q\mathbf{D} | Q = 0 \text{ for } \mathbf{X} \in \Gamma_{\text{o}},\ Q = 1 \text{ for } \mathbf{X} \in \Gamma_{\delta}\}. \tag{23}$$

The function space $\mathcal{Q}$ introduces the condition $Q = 1$ on Γ_{δ} that in the limit $\delta \to 0$ represents an imposed trial extension of the crack along the direction $\mathbf{D}$. The condition $Q = 0$ on Γ_{o} can be viewed as holding fixed the configuration of the external boundary and crack surfaces. The local balance of energy–momentum Eq. (9) is multiplied through by $\mathbf{Q}$. The result is integrated by parts over the regular part of the body Ω_{r} to give

$$\int_{\Omega_{\text{r}}} -\boldsymbol{\Sigma} : \boldsymbol{\nabla}\mathbf{Q}\, \mathrm{d}V - \int_{\Omega_{\text{r}}} -\boldsymbol{\sigma}^{\text{NEQ}} : (\boldsymbol{\nabla}\boldsymbol{\varepsilon}^{\text{v}}\mathbf{Q})\, \mathrm{d}V = \int_{\Gamma_{\delta}} \mathbf{D} \cdot \boldsymbol{\Sigma}\mathbf{N}\, \mathrm{d}S, \text{ for all } \mathbf{Q} \in \mathcal{Q}. \tag{24}$$

Assuming that $\mathbf{D}$ is the growth direction, the near-tip driving force is recovered on the right-hand side of Eq. (24) in the limit as $\delta \to 0$. The left-hand side then resembles a domain integral for the vectorial J-integral with an added domain term of viscous body forces. Factoring out $\mathbf{D}$ results in the following material force balance:

$$\int_{\Omega_{\text{r}}} -\boldsymbol{\Sigma}\boldsymbol{\nabla}Q\, \mathrm{d}V - \int_{\Omega_{\text{r}}} -\boldsymbol{\sigma}^{\text{NEQ}} : \boldsymbol{\nabla}\boldsymbol{\varepsilon}^{\text{v}} Q\, \mathrm{d}V = \int_{\Gamma_{\delta}} \boldsymbol{\Sigma}\mathbf{N}\, \mathrm{d}S. \tag{25}$$

Comparing Eqs. (10) and (25) shows that the domain expression for the global material force equivalently can be defined as

$$\mathbf{F}^{\text{mat}} = \lim_{\delta \to 0} \int_{\Omega_{\text{r}}} -\boldsymbol{\Sigma}\boldsymbol{\nabla}Q\, \mathrm{d}V - \int_{\Omega_{\text{r}}} -\boldsymbol{\sigma}^{\text{NEQ}} : \boldsymbol{\nabla}\boldsymbol{\varepsilon}^{\text{v}} Q\, \mathrm{d}V. \tag{26}$$

An approximation for the test function Q is constructed from the finite element shape functions $M_A(\mathbf{X})$ as

$$Q^h(\mathbf{X}) = \sum_{A\in\mathbb{A}_o} M_A(\mathbf{X}) Q_A, \tag{27}$$

where $\mathbb{A}_o$ is the set of all nodes in Ω_o^h. Substituting Eq. (27) into Eq. (26) produces the following Galerkin approximation for the global material force:

$$\mathbf{F}^{\mathrm{mat},h} = \sum_{A\in\mathbb{A}_o} Q_A \left(\int_{\Omega_o^h} -\boldsymbol{\Sigma}^h : \boldsymbol{\nabla} M_A \,\mathrm{d}V - \int_{\Omega_o^h} -\boldsymbol{\sigma}^{\mathrm{NEQ},h} : \boldsymbol{\nabla}\boldsymbol{\varepsilon}^{\mathrm{v},h} M_A \,\mathrm{d}V \right), \tag{28}$$

where the area Ω_δ^h has been shrunk to the nodes forming the crack tip. The expression in Eq. (28) motivates the definition of nodal material and dissipation forces

$$\begin{aligned} \mathbf{F}_A^{\mathrm{mat}} &= \mathop{\mathsf{A}}_{e=1}^{n_{\mathrm{el}}} \int_{\Omega^{\mathrm{e}}} -\boldsymbol{\Sigma}^h \boldsymbol{\nabla} M_A \,\mathrm{d}V - \mathbf{F}_A^{\mathrm{dissip}}, \\ \mathbf{F}_A^{\mathrm{dissip}} &= \mathop{\mathsf{A}}_{e=1}^{n_{\mathrm{el}}} \int_{\Omega^{\mathrm{e}}} -\boldsymbol{\sigma}^{\mathrm{NEQ},h} : \boldsymbol{\nabla}\boldsymbol{\varepsilon}^{\mathrm{v},h} M_A \,\mathrm{d}V, \end{aligned} \tag{29}$$

where Ω^{e} is the element volume, and the symbol A denotes an assembly of element nodal values. Consequently, the global material force is equal to the sum of the corresponding nodal material forces weighted by the nodal values of the test function as

$$\mathbf{F}^{\mathrm{mat},h} = \sum_{A\in\mathbb{A}_o} Q_A \mathbf{F}_A^{\mathrm{mat}}. \tag{30}$$

The global dissipation force defined in Eq. (11) can be calculated from the nodal dissipation forces simply as

$$\mathbf{F}^{\mathrm{dissip},h} = \sum_{A\in\mathbb{A}_o} \mathbf{F}_A^{\mathrm{dissip}}. \tag{31}$$

The weighted sum expression for the global material force in Eq. (30) is a consequence of the explicit consideration of the crack in obtaining the material force balance in Eq. (25). In contrast, the method of Steinmann et al. (2001) employs a space of test functions that only assembles over elements connected to the crack tip node. They interpret the resulting nodal value as the energy release rate. A modified method presented by Denzer et al. (2003) performs the assembly over the entire body Ω_o^h, then sums the resulting nodal material forces to obtain the global material force. The result is the material force expression in Eq. (30) where $Q_A = 1$.

In the elastic case, the global material force in Eq. (28) is equivalent to the domain integral method first presented by Li et al. (1985) and further developed by Shih et al. (1986) and Moran and Shih (1987). Like the domain integral method, the material force method does not restrict the variation of the test function in the integration domain Ω_{r} except to preserve smoothness conditions for differentiation and integration. Shih et al. (1986) showed in their study that calculations of the domain integral for suitably large domains were insensitive to the choice of weight functions.

The errors observed for calculations over smaller domains were caused by poor numerical resolution of the crack-tip fields. Likewise, we expect calculations of the domain expression for the global material force to be insensitive to the choice of test functions.

The final numerical issue to be addressed is the evaluation of the gradient of viscous strain in the global dissipation force. Internal variables are computed only at the integration points in the standard displacement formulation of the finite element method. A simple method for obtaining the gradient involves first extrapolating the internal variables to the nodes. Then, standard finite element interpolation are used to calculate the gradient from the extrapolated nodal values. An L_2 projection scheme widely used for stress smoothing is proposed for the extrapolation step. This method does not alter the finite element formulation and is simple to implement in an existing finite element program. Given values of $\boldsymbol{\varepsilon}^{\mathrm{v},h}$ and the shape function M_A at the integration points, the nodal values $\boldsymbol{\varepsilon}^{\mathrm{v}}_A$ are determined as,

$$\boldsymbol{\varepsilon}^{\mathrm{v}}_A = \sum_B H^{-1}_{AB} \int_{\Omega^h_{\mathrm{o}}} M_B \boldsymbol{\varepsilon}^{\mathrm{v},h} \,\mathrm{d}V, \quad \text{for } H_{AB} = \int_{\Omega^h_{\mathrm{o}}} M_A M_B \,\mathrm{d}V. \tag{32}$$

Since solving the linear system in Eq. (32) can be costly, a lumped approximation is used for the mass matrix H_{AB}. Alternatively, the extrapolation can be performed element-by-element using

$$\boldsymbol{\varepsilon}^{\mathrm{v},e}_a = \sum_b h^{e-1}_{ab} \int_{\Omega_e} M_b \boldsymbol{\varepsilon}^{\mathrm{v},h} \,\mathrm{d}V, \quad \text{for } h^e_{ab} = \int_{\Omega_e} M_a M_b \,\mathrm{d}V, \tag{33}$$

where h^e_{ab} is a consistent element mass matrix. This scheme returns a discontinuous field of element nodal values. The two extrapolation schemes are compared in Section 4.3.

3. Application to elastoplasticity

Though a material force method has been developed in the previous section specifically for linear viscoelasticity, the method can be adapted to a large class of inelastic constitutive models. It is only required that the constitutive relations are associated with a free energy density and dissipation potential. To demonstrate its general nature, a material force method is developed below for associative elastoplasticity. The mathematical manipulations are independent of the constitutive model. Therefore, this section focuses on issues of physical interpretation and numerical implementation that are unique to plasticity. Again, the global material force is compared to the generalized J-integral presented in Freund and Hutchinson (1985) for steady-state growth. Because the deviatoric nature of plastic flow can lead to volumetric locking, a mixed formulation is proposed in Section 3.4 for numerical evaluation.

3.1. Material description

An internal variable description of associative elastoplasticity assumes an additive decomposition of the strain tensor into elastic and plastic parts as

$$\boldsymbol{\varepsilon} = \boldsymbol{\varepsilon}^{\mathrm{e}} + \boldsymbol{\varepsilon}^{\mathrm{p}}. \tag{34}$$

Also assumed is a free energy density $\Psi(\boldsymbol{\varepsilon}^{\mathrm{e}}, \boldsymbol{\alpha})$ where $\boldsymbol{\alpha}$ is an internal strain governing the hardening behavior. The plastic dissipation potential is

$$\mathscr{D}^{\mathrm{plastic}} = \boldsymbol{\sigma} : \dot{\boldsymbol{\varepsilon}}^{\mathrm{p}} + \mathbf{q} : \dot{\boldsymbol{\alpha}}, \tag{35}$$

where $\boldsymbol{\sigma}$ is the stress and $\mathbf{q}$ is the thermodynamic conjugate of $\boldsymbol{\alpha}$. The constitutive relations for $\boldsymbol{\sigma}$ and $\mathbf{q}$ are obtained from $\Psi(\boldsymbol{\varepsilon}^{\mathrm{e}}, \boldsymbol{\alpha})$ as

$$\boldsymbol{\sigma} = \frac{\partial \Psi}{\partial \boldsymbol{\varepsilon}^{\mathrm{e}}}, \quad \mathbf{q} = -\frac{\partial \Psi}{\partial \boldsymbol{\alpha}}. \tag{36}$$

To calculate the internal strains, the yield condition $f(\boldsymbol{\sigma}, \mathbf{q}) \leqslant 0$ is defined to describe an admissible stress state $\{\boldsymbol{\sigma}, \mathbf{q}\}$. Then, associative evolution equations for the internal variables $\boldsymbol{\varepsilon}^{\mathrm{p}}$ and $\boldsymbol{\alpha}$ are chosen to maximize $\mathscr{D}^{\mathrm{plastic}}$ for an admissible stress state as

$$\dot{\boldsymbol{\varepsilon}}^{\mathrm{p}} = \dot{\gamma}\frac{\partial f}{\partial \boldsymbol{\sigma}}, \quad \dot{\boldsymbol{\alpha}} = \dot{\gamma}\frac{\partial f}{\partial \mathbf{q}}. \tag{37}$$

Finally, the plastic strain rate $\dot{\gamma}$ is determined from the Kuhn–Tucker conditions $\dot{\gamma} \geqslant 0$, $f \leqslant 0$, $\dot{\gamma} f = 0$ and consistency $\dot{\gamma}\dot{f} = 0$.

3.2. Balance of energy–momentum

As in Section 2.2, the energy–momentum tensor is defined from the free energy density as

$$\boldsymbol{\Sigma} = \Psi(\boldsymbol{\varepsilon}^{\mathrm{e}}, \boldsymbol{\alpha})\mathbf{1} - \boldsymbol{\nabla}\mathbf{u}^{\mathrm{T}}\boldsymbol{\sigma}. \tag{38}$$

The resulting local balance of energy–momentum for the material motion problem is

$$\boldsymbol{\nabla} \cdot \boldsymbol{\Sigma} + \boldsymbol{\sigma} : \boldsymbol{\nabla}\boldsymbol{\varepsilon}^{\mathrm{p}} + \mathbf{q} : \boldsymbol{\nabla}\boldsymbol{\alpha} = \mathbf{0}. \tag{39}$$

The elastoplastic constitutive model produces two additional material body force terms, one for each internal variable. Each term is the product of the gradient of an internal strain and its thermodynamic conjugate stress. The local statement (39) is integrated over the regular part of the body to obtain the global balance of energy–momentum as

$$\int_{\Gamma_{\mathrm{o}}} \boldsymbol{\Sigma}\mathbf{N}\,\mathrm{d}S - \lim_{\delta \to 0}\int_{\Omega_{\mathrm{r}}} -(\boldsymbol{\sigma} : \boldsymbol{\nabla}\boldsymbol{\varepsilon}^{\mathrm{p}} + \mathbf{q} : \boldsymbol{\nabla}\boldsymbol{\alpha})\,\mathrm{d}V = \lim_{\delta \to 0}\int_{\Gamma_{\delta}} \boldsymbol{\Sigma}\mathbf{N}\,\mathrm{d}S. \tag{40}$$

From Eq. (40), the global material and dissipation forces are defined as

$$\mathbf{F}^{\text{mat}} = \int_{\Gamma_o} \boldsymbol{\Sigma}\mathbf{N}\,\mathrm{d}S - \mathbf{F}^{\text{dissip}},$$
$$\mathbf{F}^{\text{dissip}} = \lim_{\delta\to 0}\int_{\Omega_r} -(\boldsymbol{\sigma} : \boldsymbol{\nabla}\boldsymbol{\varepsilon}^{\text{p}} + \mathbf{q} : \boldsymbol{\nabla}\boldsymbol{\alpha})\,\mathrm{d}V. \tag{41}$$

The global material force in Eq. (41) is the time-continuous counterpart to the discrete path-domain integral developed by Simo and Honein (1990) for elastoplasticity. If desired, the global dissipation force can be split further into contributions from the plastic flow and hardening behavior. The ability to examine separately the effect of different inelastic mechanisms leading to fracture can be useful for models with multiple internal variables, like certain damage models, each representing a disparate material process.

If instead of the free energy density, the elastic strain energy density given by

$$U^{\text{e}} = \int_0^{\varepsilon^{\text{e}}_{ij}} \sigma_{ij}\,\mathrm{d}\varepsilon^{\text{e}}_{ij} \tag{42}$$

is used to define the energy–momentum tensor in Eq. (38), then the result is the $\hat{J}$-integral of Kishimoto et al. (1980)

$$\hat{J}_k = \int_{\Gamma_o} (U^{\text{e}}N_k - u_{i,k}\sigma_{ij}N_j)\,\mathrm{d}S + \lim_{\delta\to 0}\int_{\Omega_r} \sigma_{ij}\varepsilon^{\text{p}}_{ij,k}\,\mathrm{d}V. \tag{43}$$

The $\hat{J}$-integral lacks the hardening term of the global material force in Eq. (41) and thus, the two formulations are equivalent only for perfect plasticity.

3.3. Steady-state growth under small-scale yielding

For steady-state growth, the steady-state relations (15) are used to express the global balance of energy–momentum Eq. (40) in the crack-tip frame as

$$\int_{\tilde{\Gamma}_o} \mathbf{e}_1 \cdot \boldsymbol{\Sigma}\mathbf{N}\,\mathrm{d}S - \frac{1}{v}\lim_{\delta\to 0}\int_{\tilde{\Omega}_r} \mathscr{D}^{\text{plastic}}\,\mathrm{d}V = \lim_{\delta\to 0}\int_{\tilde{\Gamma}_\delta} \mathbf{e}_1 \cdot \boldsymbol{\Sigma}\mathbf{N}\,\mathrm{d}S, \tag{44}$$

where $\mathbf{e}_1$ is the growth direction. The boundary contour $\tilde{\Gamma}_o$ defined in the crack-tip frame intersects the plastic wake as shown in Fig. 5. For small-scale yielding, the characteristic dimension of the plastic wake h is small compared to $\tilde{\Gamma}_o$. Thus, the first term in Eq. (44) can be decoupled into the far-field energy release rate G and a work rate from the residual energy locked in the wake. Assuming $\mathbf{N} = -\mathbf{e}_1$ for the intersection of the contour and the plastic wake, Eq. (44) can be rewritten as

$$G - \frac{1}{v}\lim_{\delta\to 0}\int_{\tilde{\Omega}_r} \mathscr{D}^{\text{plastic}}\,\mathrm{d}V - \int_{-h}^{h} (\Psi - u_{i,1}\sigma_{i1})\,\mathrm{d}x_2 = G_\delta, \tag{45}$$

where G_δ is the near-tip energy release rate. As in Freund and Hutchinson (1985), it is assumed that the wake is long such that ε_{11} and σ_{12} vanish far from the crack tip.

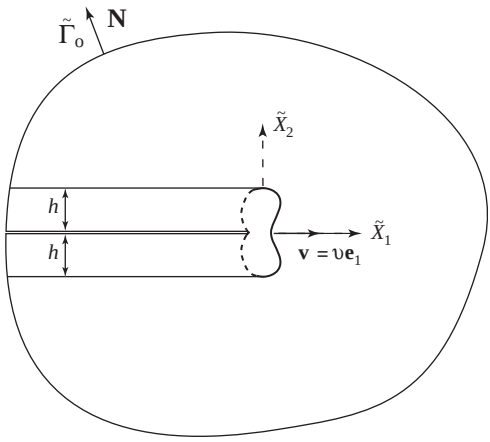

Fig. 5. Steady-state crack growth in an elastoplastic body.

This reduces the above equation to,

$$G - \frac{1}{v}\lim_{\delta\to 0}\int_{\tilde{\Omega}_r} \mathscr{D}^{\text{plastic}}\,\mathrm{d}V - \int_{-h}^{h} \Psi\,\mathrm{d}x_2 = G_\delta, \tag{46}$$

which states that the near-tip energy release rate is equal to the far-field value less the work rate of plastic dissipation and the work rate of the free energy locked in the wake. This result is a generalization of the work rate balance obtained by Freund and Hutchinson (1985) using the J-integral.

3.4. Mixed formulation

Since plastic flow is deviatoric by nature, extensive plastic deformation produces an incompressible material response that leads to volumetric locking in finite element computations. In anticipation of this problem, a mixed formulation is developed for numerical implementation. The mixed formulation uses the deviatoric–volumetric split of the strain tensor to define an independent dilatational field θ and a mixed strain tensor

$$\bar{\boldsymbol{\varepsilon}} = \boldsymbol{\varepsilon} + \tfrac{1}{3}(\theta - \operatorname{tr}\boldsymbol{\varepsilon})\mathbf{1}, \tag{47}$$

which is associated with the mixed displacement gradient expressed as

$$\boldsymbol{\nabla}\bar{\mathbf{u}} = \boldsymbol{\nabla}\mathbf{u} + \tfrac{1}{3}(\theta - \operatorname{tr}\boldsymbol{\varepsilon})\mathbf{1}. \tag{48}$$

The constraint $\theta = \operatorname{tr}\boldsymbol{\varepsilon}$ is enforced through a local Lagrange multiplier p that is the pressure.

When applied to elastoplasticity, the mixed formulation affects only $\boldsymbol{\varepsilon}^{\mathrm{e}}$ since $\boldsymbol{\varepsilon}^{\mathrm{p}}$ is by definition deviatoric. The mixed free-energy density is defined using $\bar{\boldsymbol{\varepsilon}}^{\mathrm{e}}$ and the

mixed stress is calculated as

$$\bar{\boldsymbol{\sigma}} = \frac{\partial \Psi(\bar{\boldsymbol{\varepsilon}}^{\mathrm{e}}, \boldsymbol{\alpha})}{\partial \bar{\boldsymbol{\varepsilon}}^{\mathrm{e}}}. \tag{49}$$

Carrying out the developments in Section 3.2 using the mixed quantities produces the following expressions for the global material and dissipation forces:

$$\begin{aligned} \mathbf{F}^{\mathrm{mat}} &= \int_{\Gamma_{\mathrm{o}}} \bar{\boldsymbol{\Sigma}}\mathbf{N}\,\mathrm{d}S - \mathbf{F}^{\mathrm{dissip}}, \\ \mathbf{F}^{\mathrm{dissip}} &= \lim_{\delta \to 0} \int_{\Omega_{\mathrm{o}}} -(\bar{\boldsymbol{\sigma}} : \boldsymbol{\nabla}\boldsymbol{\varepsilon}^{\mathrm{p}} + \mathbf{q} : \boldsymbol{\nabla}\boldsymbol{\alpha})\,\mathrm{d}V, \end{aligned} \tag{50}$$

where the mixed energy–momentum tensor is

$$\bar{\boldsymbol{\Sigma}} = \Psi(\bar{\boldsymbol{\varepsilon}}^{\mathrm{e}}, \boldsymbol{\alpha})\mathbf{1} - \boldsymbol{\nabla}\bar{\mathbf{u}}^{\mathrm{T}}\bar{\boldsymbol{\sigma}}. \tag{51}$$

Alternatively, the expression for the mixed energy–momentum tensor can be obtained from the material variation of the mixed Lagrangian for the incompressible hyperelastic problem, then linearized for use in a small-strain setting.

4. Numerical examples

The material force method is applied to calculate the fracture energy and work rate of dissipation for Mode I fracture in an applied K-field for viscoelasticity and J_2 elastoplasticity. Crack growth is modeled using cohesive surfaces. The viscoelastic problem is used to compare the choice of discretization methods in combination with various schemes for computing strain gradients. The elastoplastic problem is applied to study the influence of cohesive and bulk properties on the plastic dissipation for crack initiation and steady-state growth. This problem was studied by Tvergaard and Hutchinson (1992), where they showed that the energy release rate at steady state as determined from the applied K-field varied sharply with the ratio of the cohesive and yield strengths, the hardening modulus, and the cohesive energy, and that the applied energy release rate at initiation depended only on the cohesive energy. These conclusions are examined here as they pertain to the plastic dissipation using the global dissipation force.

4.1. The finite element geometry

The finite element (FE) mesh developed for the cohesive fracture problem is shown in Fig. 6. The mesh geometry is a disk of radius L with a radial pre-crack described by $X_1 < 0$ for $X_2 = 0$. The surfaces of the pre-crack are traction free. Plane strain conditions are imposed in all cases. Ahead of the pre-crack is a region uniformly meshed by square elements of size h. For the viscoelastic problem $L = 1000h$ and the size of the uniformly meshed region is $W = 100h$. For the elastoplastic problem, the dimensions of the mesh are enlarged to $L = 4000h$ and $W = 200h$ to obtain small-scale yielding conditions.

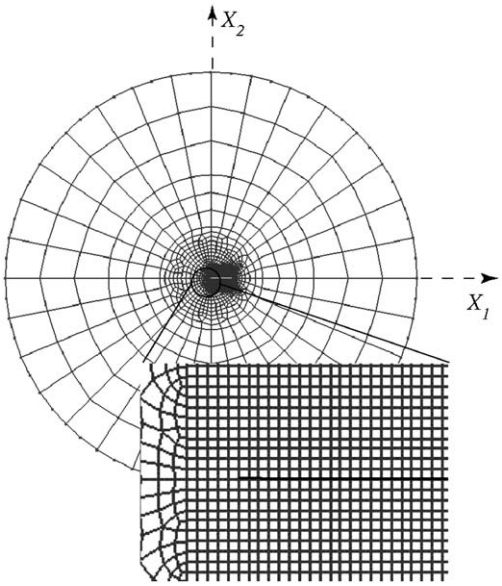

Fig. 6. The finite element geometry for cohesive fracture in an applied K-field.

Displacements consistent with a Mode I K-field are applied to the external boundary of the disk. They can be written in terms of radial coordinates calculated from the crack tip as

$$\mathbf{u}(r,\theta) = \frac{K_{\mathrm{I}}}{E^*}\sqrt{\frac{r}{2\pi}}\boldsymbol{f}(\theta), \tag{52}$$

where $\boldsymbol{f}(\theta)$ is the plane strain function of the angular variation for the Mode I K-field. For the viscoelastic problem, E^* is the plane strain equilibrium modulus while it is the plane strain elastic modulus for the elastoplastic problem. The far-field strain energy release rate provided by the applied K-field is

$$G = \frac{K_{\mathrm{I}}^2}{E^*}. \tag{53}$$

Inserted along the crack plane at $0 \leqslant X_1 \leqslant W$ are cohesive surfaces for which the constitutive behavior is prescribed by the Xu and Needleman (1994) model. The traction-separation law of the isotropic Xu–Needleman model for Mode I opening can be expressed as

$$T_{\mathrm{n}}(\Delta_{\mathrm{n}}) = \frac{\phi_{\mathrm{n}}\Delta_{\mathrm{n}}}{\delta_{\mathrm{n}}^2}\exp\left(-\frac{\Delta_{\mathrm{n}}}{\delta_{\mathrm{n}}}\right), \tag{54}$$

where T_{n} and Δ_{n} are the normal traction and surface separation, ϕ_{n} is the opening mode cohesive energy, and δ_{n} is the critical separation for maximum T_{n}. The cohesive energy ϕ_{n} is used to verify the calculations for the global material force. The difference between the cohesive energy and the global energy release rate in Eq. (53)

provides a comparison for the global dissipation force. For elastoplasticity, this comparison is exact only if negligible free energy is trapped in the plastic wake by crack growth. The residual free energy in the wake can be detected by the appearance of nodal material forces behind the cohesive zone, above the crack plane. They can be summed to the global dissipation force as directed by Eq. (46) to correct for any discrepancies.

The finite element equations are solved using a Newton Raphson scheme. For each iteration, an initial solution is sought for the applied boundary conditions. The position of the crack tip is calculated by searching along the crack plane for the point of maximum stress. If motion of the tip is detected, a relaxation step is conducted in which the boundary conditions are adjusted to center the applied K-field about the new tip position. A solution for the updated boundary conditions is determine, and a search is executed again for the crack tip position. The relaxation step is repeated until crack motion ceases to be detected. Backward motion, though detected, is prohibited to prevent spurious healing during the solution process. The simulation is allowed to progress until steady-state conditions are established. Steady-state growth is marked by diverging solutions of crack extension for vanishingly small increases in the stress intensity factor. Crack growth is distinguished from tip motion in the simulations. The crack tip can move from the evolution of the cohesive zone. However, initiation of crack growth is discerned only when the surface work of separation equals 99% of the cohesive energy ϕ_{n}. In terms of the crack opening, the initiation criterion corresponds to $\Delta_{\mathrm{n}} = 7\delta_{\mathrm{n}}$.

4.2. Viscoelastic cohesive fracture

For the viscoelastic problem, the ratio of the long- and short-time moduli and Poisson's ratio are chosen as $E_\infty/E_{\mathrm{o}} = 0.5$ and $\nu = 0.33$, The characteristic relaxation time τ for both the shear and bulk response is set to 0.0025 s. The cohesive properties, $\delta_{\mathrm{n}}/h = 0.12$, $\sigma_{\mathrm{n}} = E_{\mathrm{o}}/15$, are chosen such that the cohesive zone size, defined by the decreasing tail of the traction-separation law, is resolved well by the mesh throughout the duration of growth. The applied rate of stress intensity factor in relation to the relaxation time is $\dot{K}_{\mathrm{I}}\tau = 0.01\sqrt{E_\infty \phi_{\mathrm{n}}/(1-\nu^2)}$. The initiation time implied by the applied loading rate is significantly larger than τ. This slow loading rate allows the material in the crack tip region to be fully relaxed at initiation.

Biquadratic Lagrangian elements are used for the calculations and the smooth extrapolation scheme expressed by Eq. (32) is applied to compute the gradient of the internal viscous strain. The lumped mass matrix H_{AB} employed by the extrapolation scheme is calculated by a simple row summing technique. Fig. 7 shows the field of nodal material forces near the crack tip as determined from Eq. (29). The magnitude of $\mathbf{F}_A^{\mathrm{mat}}$ is significant only at the nodes forming the cohesive zone. Small values away from the crack tip have been attributed by Steinmann et al. (2001) to errors introduced by the element discretization. The nodal material forces in the cohesive zone are aligned primarily with the growth direction to indicate energy flow to the crack tip. The field of nodal dissipation forces is shown in Fig. 8. The results have

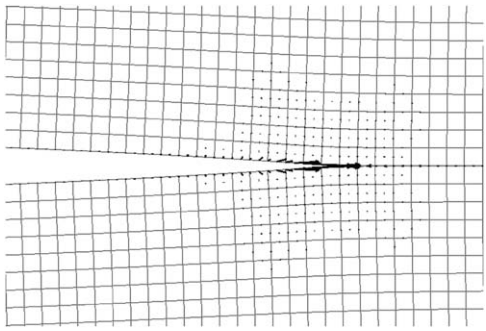

Fig. 7. Field of nodal material forces for the viscoelastic problem.

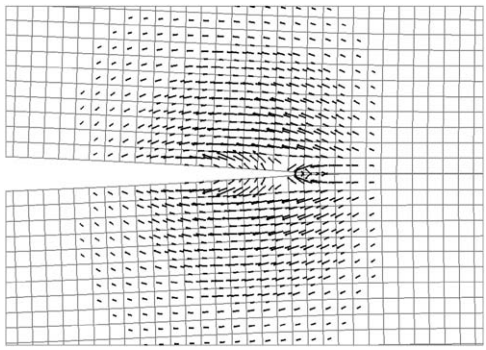

Fig. 8. Field of nodal dissipation forces for the viscoelastic problem.

been filtered to remove the smaller values so that the overall distribution can be viewed more clearly. The nodal dissipation forces visualize a "peanut" shape region about the crack tip that is interpreted as the viscous dissipation zone. In contrast to the nodal material forces, the nodal dissipation forces are directed in opposition to crack motion.

Following Eq. (30), the component of $\mathbf{F}_A^{\text{mat}}$ in the growth direction is summed for $Q_A = 1$ everywhere but on the external boundary to give F_1^{mat}. For this choice of Q_A, the test function $Q(\mathbf{X})$ has a "plateau" shape that decreases linearly from one to zero in outermost layer of elements away from the crack tip. The component of the nodal dissipation forces $\mathbf{F}_A^{\text{dissip}}$ in the growth direction is summed according to Eq. (31) to give F_1^{dissip}. The time histories of F_1^{mat}/ϕ_n and $F_1^{\text{dissip}}/\phi_n$ are plotted in Fig. 9 where time is normalized by the initiation time t_f. Also included in the figure for comparison is the history of the global energy release rate G/ϕ_n calculated from Eq. (53). Before initiation $t < t_f$, $F_1^{\text{dissip}} = 0$ and $F_1^{\text{mat}} = G$. Both results conform to the expectation that little dissipation would be generated for the static crack by the slow loading rate. As the crack opens and the cohesive zone begins to grow, F_1^{dissip} increases slightly. After initiation $t \geqslant t_f$, F_1^{mat} converges to the cohesive energy while

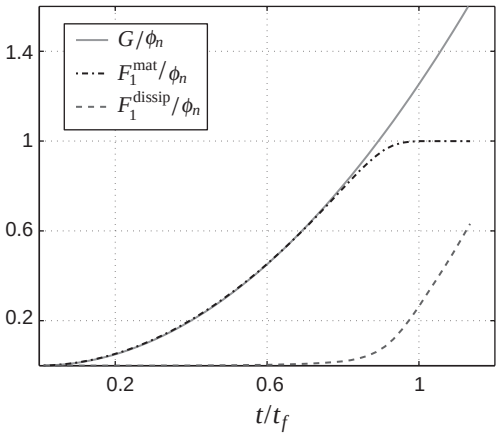

Fig. 9. The global material and dissipation forces in the growth direction for the viscoelastic problem.

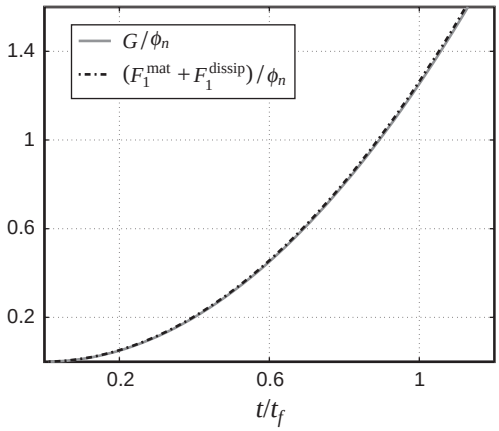

Fig. 10. Comparing the computed and applied global driving force for the viscoelastic problem.

F_1^{dissip} grows with G. The far-field energy release rate is recovered by the sum of F_1^{dissip} and F_1^{mat} as shown in Fig. 10.

4.3. Effects of element discretization and extrapolation method

Having validated the method for the viscoelastic problem, the effects of element discretization and extrapolation method are now examined. The viscoelastic fracture problem is solved using bilinear Lagrangian (L4), biquadratic Serendipity (S8), and biquadratic Lagrangian (L9) elements. Material forces are computed using the same element types in conjunction with the smooth (S) and discontinuous (D) extrapolation schemes. The S8–S case is excluded from study because the lumped mass matrix H_{AB} calculated using the row summing technique for the S8 element

contains negative diagonal components. The L9–S case is the same as the validation problem. Its results are used as benchmarks in the following discussion. The time histories of F_1^{mat} and F_1^{dissip} are shown in Fig. 11 for all cases. The calculations exhibit minor differences before initiation since viscous dissipation is produced only with crack growth for the specified loading rate. However, it is clear that accuracy is improved by higher order discretization for the growing crack. The L4–S case consistently overestimates F_1^{mat} and underestimates F_1^{dissip}, though the errors are relatively small. Results for the L4–D case exhibit the wrong trend for both the global material and dissipation forces. After initiation, F_1^{mat} grows in time instead of converging to the cohesive energy, and F_1^{dissip} severely lags the benchmark. The poor performance of the L4–D case is attributed to the inappropriate use of the discontinuous extrapolation scheme in combination with the bilinear element discretization that cannot represent higher order derivatives. The sum $F_1^{\text{mat}} + F_1^{\text{dissip}}$ plotted in Fig. 11(c) for all cases are indistinguishable. Since the sum represents a domain integral for the far-field energy release rate, the agreement in Fig. 11(c) indicates that the accuracy of the finite element fields is comparable for all the

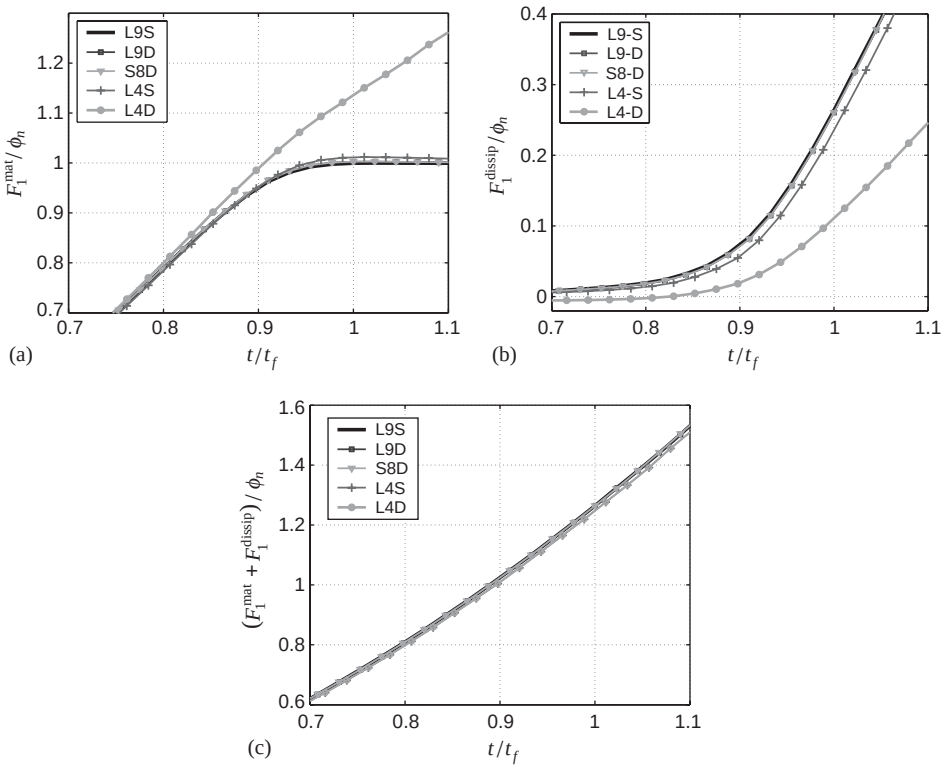

Fig. 11. Comparing element types and extrapolation schemes for: (a) the global material force, (b) the global dissipation force, and (c) their sum.

element types. Thus, errors in the material force calculations must originate from calculations of the gradient of viscous strain.

Fig. 12 shows the field of nodal dissipation forces $\mathbf{F}_A^{\text{dissip}}$ near the crack tip for all combinations of element discretization and extrapolation schemes. The general characteristics of the fields are similar for all but the L4–D case. However, the particular distribution of nodal forces within an element depends strongly on the element discretization. This dependence is unavoidable because the nodal dissipation forces are calculated by projecting the global dissipation force onto the finite element

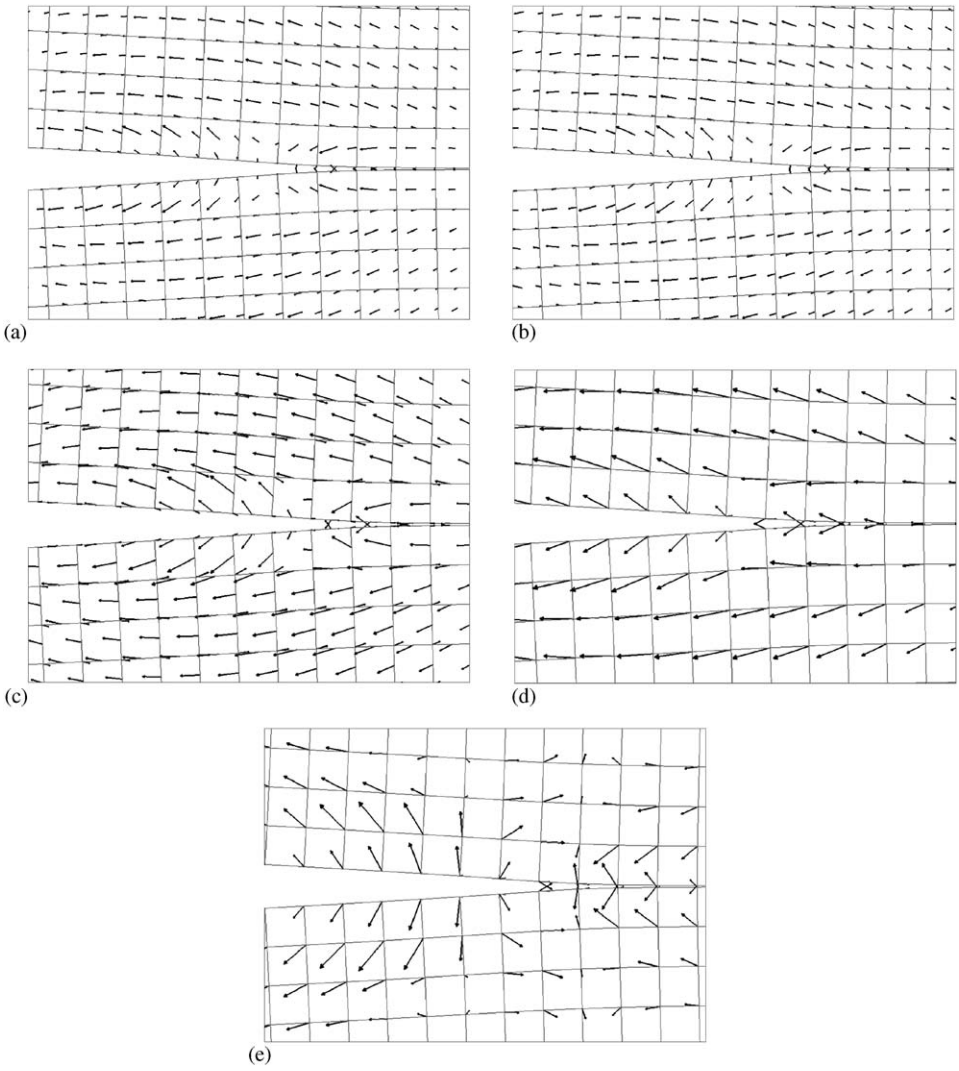

Fig. 12. Vector field of nodal dissipation forces for different combinations of element discretization and extrapolation schemes: (a) L9-S, (b) L9-D, (c) S8-D, (d) L4-S, (e) L4-D.

solution space. For an L9 element, the largest magnitude appears at the center node. The forces on the mid-side nodes of an S8 element are oriented opposite to those on the corner nodes, and are greater in magnitude. The results of Figs. 11 and 12 show that the global extrapolation scheme is necessary for use with the bilinear element. However, its effect is minor when paired with higher order elements.

4.4. Elastoplastic cohesive fracture

Simulations of cohesive fracture in an elastoplastic body are conducted to validate the mixed formulation presented in Section 3.4. The mixed formulation is implemented using Q1/P0 elements and a global extrapolation scheme is applied to compute gradients of the internal plastic variables. The Q1/P0 element approximates the displacement field using bilinear shape functions and enforces a piecewise constant pressure field. The elastoplastic model is characterized by a J_2 flow rule and a linear, isotropic hardening function. The hardening modulus is $H/E = 0.05$, and the yield strength is set to $\sigma_Y = 0.0019E$. The cohesive properties are chosen such that $\sigma_n/\sigma_Y = 3.5$, $\delta_n = 0.12h$, and $r_Y = 73h$ where the plastic zone size r_Y is determined from Tvergaard and Hutchinson (1992, Eq. (1.9)) as,

$$r_Y = \frac{1}{3\pi}\frac{E^*\phi_n}{\sigma_Y^2}. \tag{55}$$

Results show that the length of the cohesive zone for the given combination of bulk material and cohesive properties is well resolved by the FE mesh throughout growth.

The field of nodal material forces near the crack tip is shown in Fig. 13. The corresponding field of nodal dissipation forces is presented in Fig. 14. The growing crack tip appears on the far right in both figures while the original crack tip at $X_1 = 0$ is shown on the far left. The latter can be identified by a slight curve in the crack surfaces caused by crack-tip blunting prior to initiation. Aside from appearing in the cohesive zone, significant values of $\mathbf{F}_A^{\text{mat}}$ also exists around the blunted region of the original crack tip. These nodal material forces are attributed to the free energy trapped in the plastic wake at initiation. The majority are oriented normal to the

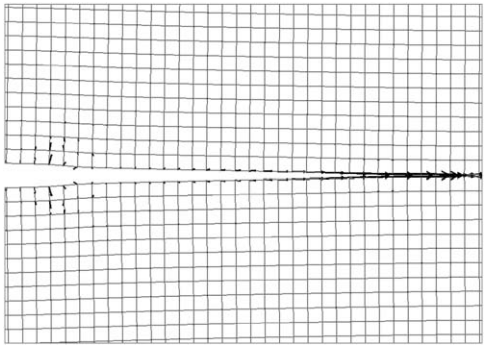

Fig. 13. Field of nodal material forces for the elastoplastic problem.

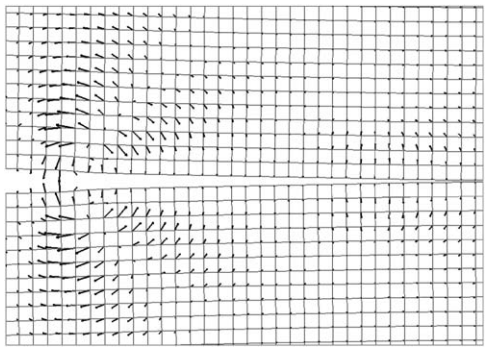

Fig. 14. Field of nodal dissipation forces for the elastoplastic problem.

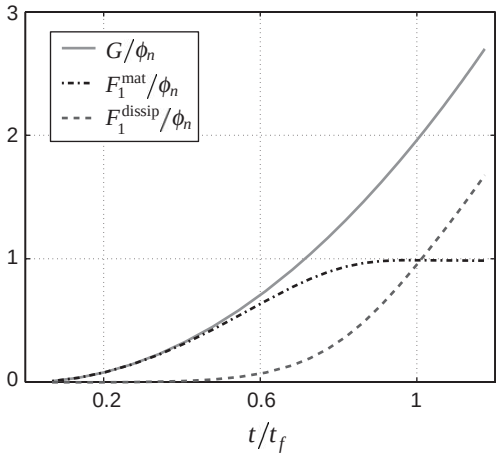

Fig. 15. The global material and dissipation forces in the growth direction for the elastoplastic problem.

crack plane and do not contribute to the global material force. In contrast, the nodal dissipation forces near the original crack tip are large and oriented mostly against the growth direction. This indicates that initiation is accompanied by significant plastic dissipation. The nodal dissipation forces about the current crack tip are generally smaller and uniformly opposed to the growth direction. Moreover, they decay as the crack tip grows past the surrounding material. As a result, only small values of the nodal dissipation forces are found in the region between the original and current tip positions.

The time histories of F_1^{mat}, F_1^{dissip}, and G as obtained from Eq. (53) are shown in Fig. 15. Unlike for the viscoelasticity example, F_1^{dissip} is significant for $t<t_f$ which demonstrates extensive plastic deformation preceding initiation. Initially when F_1^{dissip} is small, the component F_1^{mat} equals the far-field energy release rate G. It accurately evaluates the cohesive energy after initiation for $t>t_f$. The sum $F_1^{\text{mat}}+F_1^{\text{dissip}}$ and the global energy release rate are compared in Fig. 16. The two are equivalent which

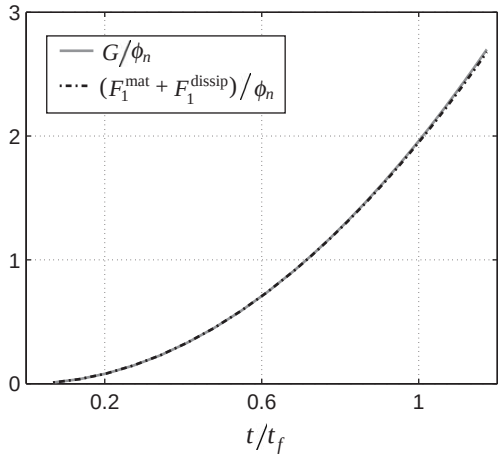

Fig. 16. Comparing the computed and applied global driving force for the elastoplastic problem.

confirms that only a negligible amount of free energy becomes trapped in the wake as a result of crack growth.

4.5. *Influence of cohesive and bulk material properties on the plastic dissipation*

Results of the elastoplastic validation problem show that for $\sigma_n/\sigma_Y = 3.5$ and $H/E = 0.05$, the plastic dissipation at initiation is comparable to the cohesive energy. It is nearly double the cohesive energy for steady-state growth. To investigate further the influence of cohesive and bulk material properties on the plastic dissipation, the elastoplastic fracture problem is examined for different values of σ_n/σ_Y and H/E.

The bulk elastic and the cohesive properties in this study are fixed for better control of the cohesive zone size relative to h. Consequently, varying σ_n/σ_Y directly changes the size of the plastic zone. For $2.5 \leqslant \sigma_n/\sigma_Y \leqslant 4.0$, the plastic zone size spans $73h \leqslant r_Y \leqslant 96h$. Fig. 17 plots the plastic dissipation calculated by $F_1^{\text{dissip}}/\phi_n$ as a function of crack growth $\Delta a/r_Y$ for $H/E = 0.05$ and different values of σ_n/σ_Y. The calculations are allowed to proceed until steady-state growth is achieved. Plots of F_1^{dissip} as a function of Δa confirm a leveling of the plastic dissipation prior to steady-state growth for all cases. As shown in Fig. 17, crack growth in the transient period can be small compared to the plastic zone size. For a given H/E, the amount of crack growth needed to reach steady-state increases with σ_n/σ_Y.

The plastic dissipation at initiation $F_{1,f}^{\text{dissip}}$ is plotted in Fig. 18 as a function of σ_n/σ_Y for different H/E. The results contradict the conclusions of Tvergaard and Hutchinson (1992) that plastic dissipation is absent at initiation. Significant plastic dissipation is obtained in these simulations because the cohesive zone is well resolved by the FE mesh. For $\sigma_n/\sigma_Y < 2.5$, $F_{1,f}^{\text{dissip}}$ is small compared to ϕ_n. However, $F_{1,f}^{\text{dissip}}$ increases for larger values of σ_n/σ_Y. The rise in $F_{1,f}^{\text{dissip}}$ corresponds to an increase in the plastic zone size with σ_n/σ_Y. In addition, a lower yield strength σ_Y inhibits crack

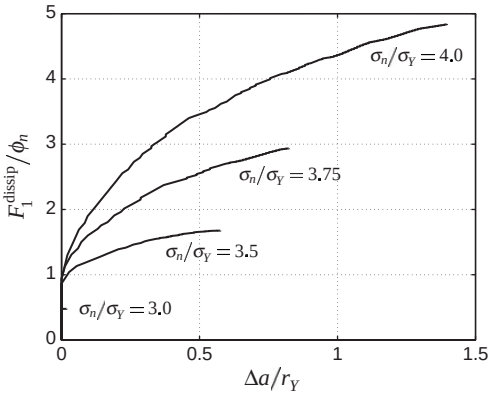

Fig. 17. The plastic dissipation as a function of crack growth for $H/E = 0.05$ and different values of σ_n/σ_Y.

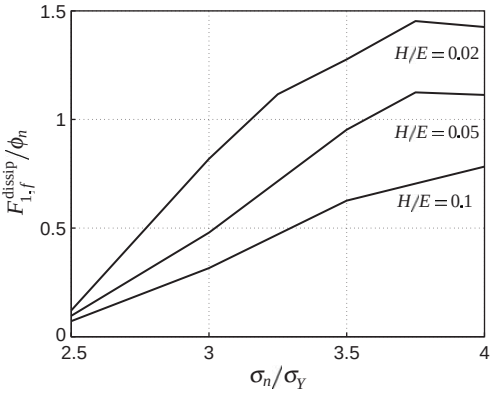

Fig. 18. The plastic dissipation at initiation as a function of σ_n/σ_Y for different values of strain hardening.

growth by preventing the normal traction on the crack plane σ_{22} from attaining the peak value σ_n. This allows more plastic dissipation to develop in the bulk material before initiation. A greater increase in $F_{1,f}^{\text{dissip}}$ is observed for lower levels of strain hardening. Hardening promotes an increase in σ_{22} on the crack plane, and a large ratio of H/E allows a crack to initiate before a significant plastic zone can form. For these reasons, it is expected that $F_{1,f}^{\text{dissip}}$ increases monotonically with σ_n/σ_Y and decreases with H/E. However, Fig. 18 demonstrates a different trend in $F_{1,f}^{\text{dissip}}$ for $\sigma_n/\sigma_Y > 3.75$ and $H/E \leqslant 0.05$. The changing trend most likely is related to issues of mesh resolution. Severe blunting caused by extensive plastic flow in the crack-tip region can shrink the cohesive zone to below the size at which the FE mesh can reproduce the distribution of cohesive traction and the resulting cohesive energy. Moreover, the mesh cannot calculate accurately the plastic dissipation in the bulk material if it is unable to resolve the extent of crack-tip blunting. A convergence

study is needed to determine if the element size h as a ratio of critical crack opening is sufficient to represent accurately the plastic deformation in the near-tip region.

Fig. 19 shows the effects of σ_n/σ_Y and H/E on the steady-state value of the plastic dissipation $F_{1,ss}^{dissip}$. Like for initiation, $F_{1,ss}^{dissip}$ is small for $\sigma_n/\sigma_Y < 3.0$. However, it unambiguously increases with σ_n/σ_Y and decreases with H/E. The growth in $F_{1,ss}^{dissip}$ reflects an increase in plastic zone size with σ_n/σ_Y. Moreover, lower yield strengths and hardening moduli permit the plastic zone to develop more fully before the onset of steady-state growth. Fig. 20 plots the length of the cohesive zone for steady-state growth δ_{ss}. The cohesive zone is defined by the decaying tail of the traction-separation law defined by $\delta_n \leqslant \Delta_n \leqslant 7\delta_n$. Recall that the surface work equals 99% of the cohesive energy for $\Delta_n = 7\delta_n$. As expected, smaller cohesive zones are obtained for larger values of σ_n/σ_Y and smaller values of H/E because of crack blunting. For $H/E = 0.02$ and $\sigma_n/\sigma_Y = 4.0$, the cohesive zone spans only seven elements. Hence,

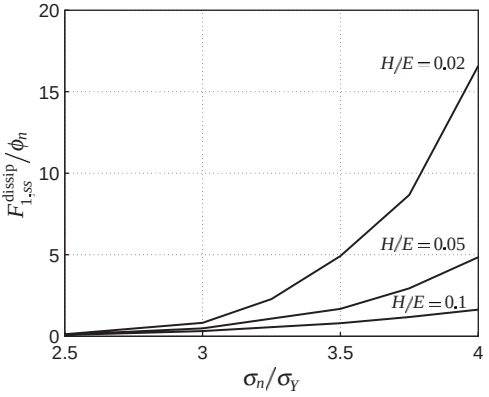

Fig. 19. Plastic dissipation for steady-state growth as function σ_n/σ_Y for different strain hardening levels.

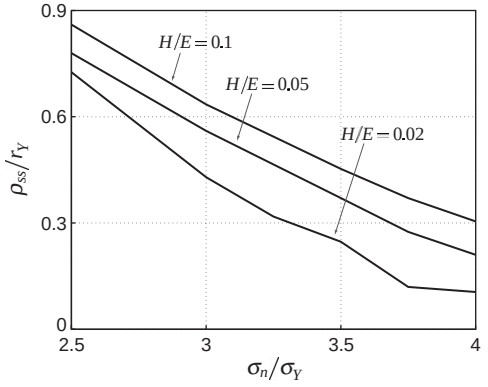

Fig. 20. Cohesive zone length for steady-state growth as function σ_n/σ_Y for different strain hardening levels.

simulations for $H/E<0.02$ were not performed because it was expected that the cohesive zone size would be too small and the blunting too severe to calculate accurately the plastic dissipation.

5. Summary

A material force method was developed to calculate the energy release rate for quasi-static viscoelastic and elastoplastic fracture. The method can be adapted to a large class of inelastic material models provided that the material response is derived from explicitly defined free energy and dissipation potentials. The method provides expressions for the global material and dissipation forces that calculate the near-tip energy release rate and work rate of dissipation. Since the material force method explicitly evaluates the work rate of dissipation in the bulk material, it can be applied to general transient problems unlike past J-integral-based formulations. Further, it has been shown that the material force and J-integral methods calculate the same work rate balance for steady-state growth.

A Galerkin discretization was applied to the domain integral expressions of the global material and dissipation forces. In addition, a mixed formulation was proposed to address volumetric locking for elastoplasticity. Galerkin discretization results in approximations for the global material force that is equal to the weighted sum of nodal material forces. The discretization also leads to the definition of nodal dissipation forces, the sum of which compute the global dissipation force. The field of nodal dissipation forces provides a tool for visualizing the near-tip dissipation region. The method was applied to cohesive fracture in a viscoelastic and elastoplastic body. Results show that the global material force accurately evaluates the cohesive energy during growth. Also, the sum of the global material and dissipation forces recovers the far-field energy release rate as provided by the applied K-field.

The viscoelastic problem was used to examine the effects of element discretization and extrapolation methods on the material force calculations. For bilinear elements, a smooth extrapolation scheme is necessary to obtain physical results. Overall, a higher-order element discretization improves the accuracy of the material force method. However, the field of nodal dissipation forces exhibits more acute sensitivity to the element discretization than the aggregate global value.

The advantage of applying the material force method to the elastoplastic problem is the ability to separate contributions to the energy release rate from the plastic dissipation and the residual free energy in the wake. The plastic dissipation is calculated by the global dissipation force. The amount of the residual free energy can be identified directly from the field of nodal material forces in the wake or indirectly from the difference between the sum of the global material and dissipation forces and a known far-field energy release rate. The influence of the cohesive and bulk material properties on the plastic dissipation was examined using calculations of the global dissipation force. The results show that the dissipation for initiation and steady-state growth grows with the ratio of the cohesive to yield strength. Lower values of the

hardening modulus relative to the elastic stiffness also promote the development of plastic dissipation.

Acknowledgements

This work was supported by the National Science Foundation under the grant CMS-9979717 to Stanford University and by the US DOE at Sandia National Laboratories under the Contract DE-AC04-94AL85000.

References

Blackburn, W., 1972. Path independent integrals to predict onset of crack instability in an elastic plastic material. Int. J. Fract. 8, 343–346.

Brust, F., Atluri, S.N., 1986. Studies on creep crack growth using the T^*-integral. Eng. Fract. Mech. 23, 551–574.

Brust, F., Nishioka, T., Atluri, S.N., 1985. Further studies on elastic-plastic stable fracture utilizing the T^* integral. Eng. Fract. Mech. 22, 1079–1103.

Brust, F., McGowan, J.J., Atluri, S.N., 1986. A combined mechanical study of ductile crack growth after a large unloading, using T^*, T, and CTOA criteria. Eng. Fract. Mech. 23, 537–550.

Denzer, R., Barth, F.J., Steinmann, P., 2003. Studies in elastic fracture mechanics based on the material force method. Int. J. Numer. Methods Eng. 58, 1817–1835.

Eshelby, J.D., 1951. The force on an elastic singularity. Philos. Trans. R. Soc. London A 244, 87–112.

Eshelby, J., 1956. The continuum theory of lattice defects. In: Seitz, F., Turnbull, D. (Eds.), Progress in Solid State Physics, vol. 3. Academic Press, New York, pp. 79–144.

Eshelby, J., 1970. Energy relations and the energy–momentum tensor in continuum mechanics. In: Kanninen, M.F., Adler, W.F., Rosenfield, A.R., Jaffe, R.I. (Eds.), Inelastic Behavior of Solids. McGraw-Hill, New York, pp. 77–114.

Freund, L.B., Hutchinson, J.W., 1985. High strain-rate crack growth in rate-dependent plastic solids. J. Mech. Phys. Solids 33, 169–191.

Govindjee, S., 2004. Numerical issues in finite elasticity and viscoelasticity. In: Saccomandi, G., Ogden, R.W. (Eds.), Mechanics and Thermomechancis of Rubberlike Solids. Springer, Vienna, pp. 187–232.

Govindjee, S., Mihalic, P., 1996. Computational methods for inverse finite elastostatics. Comput. Methods Appl. Mech. Eng. 136, 47–57.

Griffith, A.A., 1920. The phenomena of rupture and flow in solids. Philos. Trans. R. Soc. A 221, 163–198.

Irwin, G.R., 1948. Fracture dynamics. In: Fracturing of Metals. American Society of Metals, Cleveland, OH, pp. 147–166.

Kishimoto, K., Aoki, S., Sakata, M., 1980. On the path independent integral $\hat{\mathrm{j}}$. Eng. Fract. Mech. 13, 841–850.

Landes, J.D., Begley, J.A., 1976. A fracture mechanics approach to creep crack growth. ASTM STP, 590, 128–148.

Li, F.Z., Shih, C.F., Needleman, A., 1985. A comparison of methods for calculating energy release rates. Eng. Fract. Mech. 21, 405–421.

Liebe, T., Denzer, R., Steinmann, P., 2003. Application of the material force method to isotropic continuum damage. Comput. Mech. 30, 171–184.

Maugin, G.A., Berezovski, A., 1999. Material formulation of finite-strain thermoelasticity and applications. J. Thermal Stresses 22, 421–449.

Maugin, G.A., Trimarco, C., 1992. Psuedomentum and material forces in nonlinear elasticity: variational formulations and application to brittle fracture. Acta Mech. 94, 1–28.

Maugin, G.A., Epstein, M., Trimarco, C., 1992. Psuedomentum and material forces in inhomogeneous materials: application to the fracture of electromagnetic materials in electromagnetoelastic fields. Int. J. Solids Struct. 29, 1889–1900.

Moran, B., Shih, C.F., 1987. Crack tip and associated domain integrals from momentum and energy balance. Eng. Fract. Mech. 27, 615–642.

Orowan, E., 1952. Fundamentals of brittle behavior of metals. In: Murray, W.M. (Ed.), Fatigue and Fracture of Metals. Wiley, New York, pp. 139–167.

Rice, J., 1968. A path-independent integral and approximate analysis of strain concentration by notches and cracks. J. Appl. Mech. 35, 379–386.

Shih, C.F., Moran, B., Nakamura, T., 1986. Energy release rate along a three-dimensional crack front in a thermally stressed body. Int. J. Fract. 30, 79–102.

Simo, J.C., Honein, T., 1990. Variational formulation, discrete conservation laws, and path-domain independent integrals for elasto-viscoplasticity. J. Appl. Mech. 57, 488–497.

Simo, J.C., Hughes, T.J.R., 1998. Computational Inelasticity. Springer, New York.

Steinmann, P., 2000. Application of material forces to hyperelastic fracture mechanics. I. Continuum mechanical setting. Int. J. Solids Struct. 37, 7371–7391.

Steinmann, P., Ackermann, D., Barth, F.J., 2001. Application of material forces to hyperelastic fracture mechanics. II. Computational setting. Int. J. Solids Struct. 38, 5509–5526.

Stumpf, H., Le, K.C., 1990. Variational principles of nonlinear fracture mechanics. Acta Mech. 83, 25–37.

Tvergaard, V., Hutchinson, J.W., 1992. The relation between crack growth resistance and fracture process parameters in elastic–plastic solids. J. Mechan. Phys. Solids 40, 1377–1397.

Xu, X.P., Needleman, A., 1994. Numerical simulations of fast crack growth in brittle solids. J. Mech. Phys. Solids 42, 1397–1434.